Supporting Information

Accelerated hydrogen evolution reaction in $Ni_3P/MoP_2/MoO_2$ tri-phase composites with rich crystalline interface and oxygen vacancies achieved by a plasma assisted phosphorization

Baoan Zhang,[a] Zhongqing Jiang,[a*] Xiaonan Shang,[a] Shasha Li,[c] and Zhong-Jie Jiang[b*]

[a] Key Laboratory of Optical Field Manipulation of Zhejiang Province, Department of Physics, Zhejiang Sci-Tech University, Hangzhou 310018, P. R. China.

[b] Guangdong Engineering and Technology Research Center for Surface Chemistry of Energy Materials & Guangzhou Key Laboratory for Surface Chemistry of Energy Materials, New Energy Research Institute, College of Environment and Energy, South China University of Technology, Guangzhou 510006, P. R. China.

[c] College of Chemical and Biological Engineering, Taiyuan University of Science and Technology, Taiyuan 030024, P. R. China.

[*]**Corresponding authors**

E-mail: zhongqingjiang@hotmail.com or zhongqingjiang@zstu.edu.cn (Z. Jiang).

E-mail: eszjiang@scut.edu.cn (Z.-J. Jiang).

This PDF file includes:

Experimental Section

Theoretical calculation details

Figures. S1 to S17

Tables S1-S4

1. Experimental Section

1.1 Chemicals

Hydrochloric acid (HCl, AR, 36.0−38.0%), ethanol (C_2H_5OH, 99.7%), nickel(II) nitrate hexahydrate ($Ni(NO_3)_2 \cdot 6H_2O$, 98%, Sigma-Aldrich), Ammonium molybdate tetrahydrate ($(NH_4)_6Mo_7O_{24} \cdot 4H_2O$, 98%, Sigma-Aldrich), sodium hypophosphite (NaH_2PO_2, 99.9%, Sigma-Aldrich), potassium hydroxide (KOH, ≥85.0%, Alfa Aesar), and Ni foam (thickness: 1.6 mm) were used as received. Ruthenium oxide (RuO_2, 99.9%) and Iridium black (Ir, 99.95%) was purchased from Alfa Aesar. Pt/C (JM 40wt % Pt-C) was purchased from Shanghai Hesen Electric Co., Ltd. Deionized water through Millipore system (Milli-Q®) was used.

1.2 Synthesis of $NiMoO_4$ nanorod arrays on Ni foam

$NiMoO_4$ nanorods (NRs) were synthesized on nickel foam ($NiMoO_4$/NF) through a hydrothermal method. Typically, a 2 × 5 cm^2 Ni foam was successively cleaned by HCl solution (4 M), ethanol, and deionized water under ultrasonication. The cleaned substrate was then placed into a Teflon-lined stainless steel autoclave (100 mL) containing a 50 mL homogenous solution of $Ni(NO_3)_2$ (0.5 mmol) and $(NH_4)_6Mo_7O_{24}$ (0.5 mmol) and hydrothermally heated at 160 °C for 4 h. After cooling, the product was thoroughly rinsed with deionized water and ethanol for several times and dried at 60 °C overnight under vacuum. The dried sample was subsequently annealed in a muffle furnace at 300 °C under the air flow for 2 h.

1.3 Synthesis of P-NiMoP nanorod arrays on Ni foam (P-NiMoP/NF)

The P-NiMoP nanorods catalyst was synthesized by one-step phosphorization of the $NiMoO_4$/NF synthesized above in a plasma enhanced chemical vapor deposition (PECVD) device equipped with a 13.56 MHz RF source. NaH_2PO_2 was used as the P source and placed at the upstream of a tube furnace. A small piece of $NiMoO_4$/NF (~ 1 cm^2) was placed at the

middle of the tube furnace in a direction perpendicular to the nitrogen (N_2) gas flow. The tube furnace was heated up to 550 ^oC with a temperature increase rate of 10 ^oC min^{-1} under vacuum. Before the plasma discharge, the plasma reaction system was evacuated to 0.1 Pa. The nitrogen gas was then introduced with the pressure controlled to 20 Pa. Then the RF power supply was turned on and the plasma discharge power was set to 100 W. The temperature was kept at 550 °C and plasma discharge was continued for 90 min. After that, RF power supply was turned off. Also, the furnace was automatically turned off and naturally cooled down to room temperature under N_2 atmosphere. For the best performing sample, the mass of NaH_2PO_2 powder was 1 g for ~ 1 cm^2 $NiMoO_4$ NRs on Ni foam.

For comparison, the T-NiMoP/NF was prepared by the conventional thermal phosphorization of the $NiMoO_4$ NRs in tube furnace at 550 °C without plasma discharge treatment under the same conditions.

1.4 Materials characterization

The morphology and crystal structure of the samples were characterized by scanning electron microscopy (SEM, Hitachi S-4800) coupled with energy dispersive X-ray (EDX) spectroscopy and transmission electron microscope (TEM, JEM-2100). The XRD patterns of the samples were obtained on an X-ray diffractometer (XRD, Bruker D8 Discover with a Cu Kα radiation at 40 KV and 40 mA). The electron paramagnetic resonance (EPR) spectra were recorded using a JES-FA200 spectrometer. X-ray photoelectron spectroscopic (XPS) measurements were performed with a Thermo Fischer ESCALAB 250Xi spectrophotometer. The Ni, Mo and P contents in the P-NiMoP and T-NiMoP nanorods were measured by a Thermo Scientific ICAP Q inductively coupled plasma mass spectrometer (ICP-MS) instrumentation. Optical emission spectra (OES) were collected on a handheld spectrometer (Ocean Optics Corporation, USA) with a spectral resolution of 0.4 nm and a detectable spectral range of 200 to 1000 nm. The Raman measurements were performed using a

LabRAM HR Evolution spectroscope (HORIBA, France) and an argon ion laser (325 nm) was used as the excitation source.

1.5 Electrochemical Tests

All electrochemical tests were performed at room temperature on an electrochemical station (CHI 760E, CH Instruments Inc., Shanghai) in a standard three-electrode system. The prepared catalysts, a graphite electrode, and a saturated calomel electrode were used as the working, the counter, and the reference electrodes, respectively. The 1.0 M KOH aqueous solution (pH = ~14) was used as the electrolyte. Before data collection, cyclic voltammetry (CV), scanned at 0.068-0.132 V vs. RHE at a scan rate of 50 mV s^{-1}, was applied to electrochemically activate the catalysts and used for the evaluation of the electrochemical stability of the catalysts.

Linear sweep voltammetry (LSV) was performed in 1.0 M KOH solution at a sweep rate of 10 mV s^{-1}. Tafel slopes were calculated based on the LSV curve by plotting overpotential (vs. the RHE) against log (current density). Electrochemical impedance spectra (EIS) were measured at an overpotential of 100 mV from 0.01 Hz to 100 KHz. All the measured potentials vs. the SCE were converted to RHE by the Nernst equation ($E_{RHE} = E_{SCE} + 0.059$ pH + 0.242). All the curves were reported with 80% iR compensation.

1.6 DFT calculations

The Vienna ab initio simulation package was employed for the DFT calculations, in which the project augmented wave method with the generalized gradient approximation in the form of Perdew-Burke-Ernzerhof was utilized to calculate the exchange-correlation interactions. The plane-wave cutoff energy of 450 eV was set. The energy and force convergence criterion were set to 10^{-5} eV and -0.01 eV $Å^{-1}$, respectively. A vacuum layer of 15 Å was chosen for the slab to eliminate the interaction between neighboring structures in the c axis. So, the dipole correction and Van der Waals correction method was not used in the calculation. The climbing image nudged elastic band (CI-NEB) method was employed to S4

calculate the minimum energy for H_2O dissociation. The Gibbs free energy of hydrogen adsorption (ΔG_{H^*}) on a surface is calculated by:

$$\Delta G_{H^*} = \Delta E_{H^*} + \Delta E_{ZPE} - T\Delta S \quad \text{(S1)}$$

where ΔE_{H^*} is the adsorption energy of hydrogen on the catalyst surface, and ΔE_{ZPE} represents the zero point energy difference between the adsorbed state and the gas phase of hydrogen atom. The higher binding energy between MoP_2/Ni_3P and MoO_2 or MoO_{2_def} is calculated.

1.7 The electrochemical active surface areas (EASAs)

The electrochemical active surface areas (EASAs) were estimated based on the electrochemical double-layer capacitance (EDLC). Generally, for a standard flat surface with a geometric surface area of 1 cm^2, the EDLC was usually at 0.02-0.06 mF cm^{-2}. It is worth noting that using nickel foam as a support has a much larger capacitance value than a flat surface as shown in **Fig. S7d**. Therefore, here Ni foam was considered as the standard. The EASA of each catalyst could be calculated according to the following formula:

$$A_{EASA} = \frac{C_{\mathrm{dl}} - catalyst\ (mF\,cm^{-2})}{C_{\mathrm{dl}} - Ni\ foam\ (mF\,cm^{-2})\,per\ EASA\ cm^2} \quad \text{(S2)}$$

Taking the P-NiMoP as an example, in the hydrogen evolution reaction, its A_{EASA} could be calculated as:

$$A_{EASA}^{P-NiMoP} = \frac{60.21\ mF\,cm^{-2}}{0.65\ mF\,cm^{-2}\,per\,cm^2_{EASA}} = 92.63\ cm^2_{EASA} \quad \text{(S3)}$$

The calculated EASA was further used in the calculation of turnover frequency.

1.8 Turnover frequency (TOF) calculations

The TOF values were calculated according to the following formula:

$$TOF = \frac{\#total\ hydrogen\ turn\ overs\ /\ geometric\ area\ (cm^2)}{\#\text{surface}\ active\ sites\ /\ geometric\ area\ (cm^2)} \quad \text{(S4)}$$

The number of the total hydrogen turnovers can be calculated based on the current density (J, IR-corrected) according to:

$$H_2 = |J| \frac{\mathrm{m}A}{cm^2} \cdot \frac{1\ C\ s^{-1}}{1000\ mA} \cdot \frac{1\ mol\ e^-}{96495.3\ C} \cdot \frac{1\ mol\ H_2}{2\ mol\ e^-} \cdot \frac{6.022\times10^{23}\ H_2\ molecules}{1\ mol\ H_2}$$

$$= 3.12\times10^{15} \frac{H_2\ s^{-1}}{cm^2}\ per \frac{mA}{cm^2} \quad \text{(S5)}$$

Note that the nature of the surface active sites is not yet understood and the exact number of hydrogen binding sites is not known, we estimated the number of the active sites based on the average atomic densities of atoms at the MoP_2 (131), Ni_3P (231) and MoO_2 (-111) facets due to the difficulty in obtaining the exact numbers of active sites.

Specifically, the surface active sites per real surface area can be calculated as following (see **Fig. S16** below for the crystal structure):

Ni_3P(231): real surface area, A= 13.369304×12.505229 nm^2sin(75.62611°), contains 14 Ni and 4 P, 18 atoms.

$$\#Surface\ sites(Ni_3P(231)) = \frac{18\ atoms\ per\ facet}{13.369304\times12.505229\ nm^2 \sin(75.62611^o)\ per\ facet}$$

$$= 1.11\times10^{13} atoms/cm^2\ real\ surface\ area \quad \text{(S6)}$$

MoP_2 (131): real surface area, A= 13.8233×11.8356 nm^2 sin(93.5809°), contains 8 Mo and 12 P, 20 atoms.

$$\#Surface\ sites(MoP_2(131)) = \frac{20\ atoms\ per\ facet}{13.8233\times11.8356\ nm^2 \sin(93.5809^o)\ per\ facet}$$

$$= 1.22\times10^{13} atoms/cm^2\ real\ surface\ area \quad \text{(S7)}$$

MoO_2(-111): real surface area, A= 5.640349×7.529668 nm^2 sin(112.78756°), contains 4 Mo and 4 O, 8 atoms.

$$\#Surface\ sites(MoO_2(-111)) = \frac{8\ atoms\ per\ facet}{5.640349\times7.529668\ nm^2 \sin(112.78756^o)\ per\ facet}$$

$$= 2.04\times10^{13} atoms/cm^2\ real\ surface\ area \quad \text{(S8)}$$

Finally, the TOF can be calculated as:

$$TOF = \frac{3.12\times10^{15}\,\frac{H_2\ s^{-1}}{cm^2}\ per\ \frac{mA}{cm^2}\times|J|}{\#surface\ active\ sites\times A_{EASA}} \tag{S9}$$

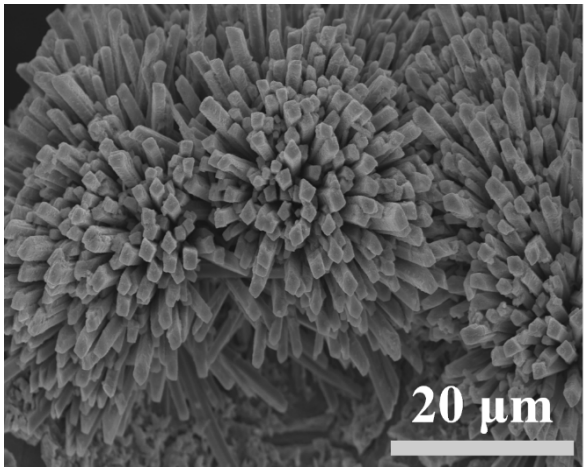

Fig. S1 SEM image of $NiMoO_4$/NF.

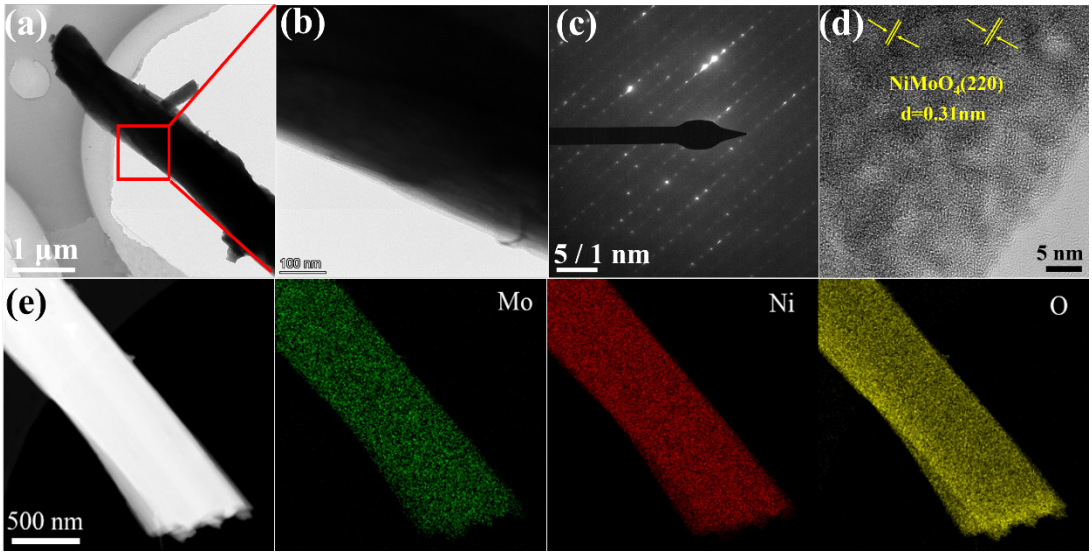

Fig. S2 (a) TEM image, (b) magnified TEM image, (c) SAED pattern, (d) HRTEM image and (e) EDX elemental mapping images of $NiMoO_4$. The energy dispersive X-ray (EDX) element mapping image shows that Ni, Mo and O elements are uniformly distributed in $NiMoO_4$ nanorods.

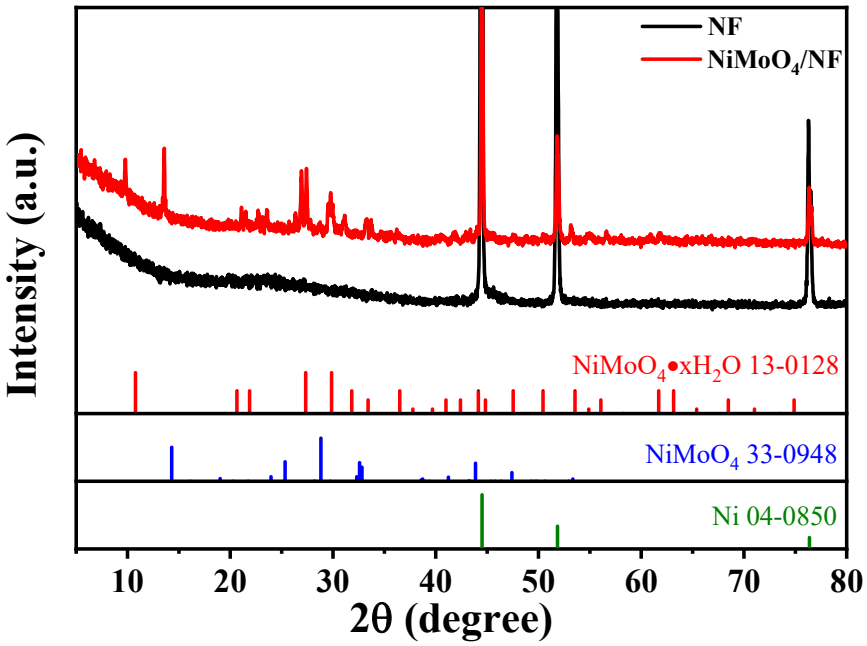

Fig. S3 XRD patterns of Ni foam and $NiMoO_4$/NF.

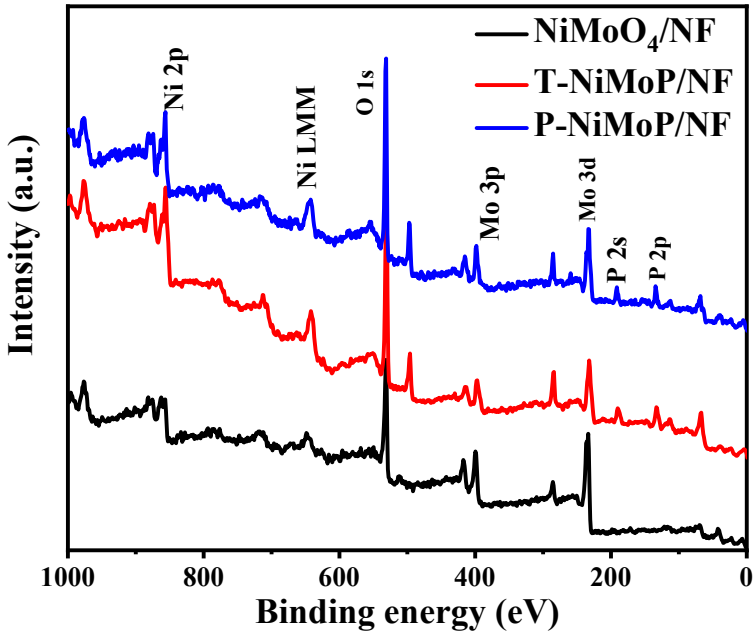

Fig. S4 XPS survey spectra of the $NiMoO_4$/NF, T-NiMoP/NF and P-NiMoP/NF.

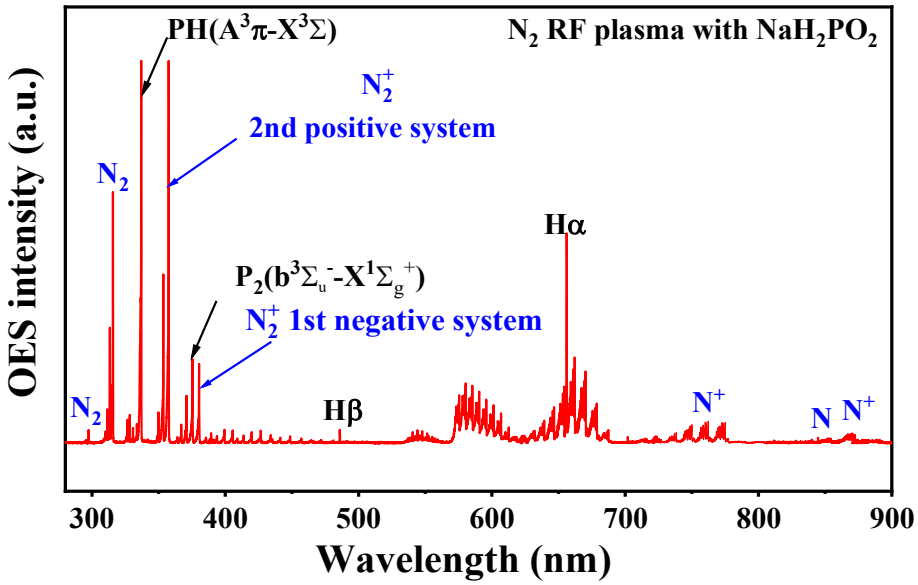

Fig. S5 Optical emission spectra of N_2 RF plasma with NaH_2PO_2. The key reactive species generated in the plasma are labelled. Plasma is essential to achieve efficient phosphorization under vacuum conditions. Optical emission spectroscopy (OES) is used to study the role of N_2 RF plasma in the phosphorization process. In the N_2 RF plasma state, there are a variety of active nitrogen including atomic nitrogen radicals and N ions (N, N^+, N_2, N_2^+). These highly reactive species will cause PH_3 produced by the pyrolysis of NaH_2PO_2 to react more violently with $NiMoO_4$ nanorods, facilitating the formation of the P-NiMoP NRs with rich crystalline interfaces and oxygen defects in MoO_2.

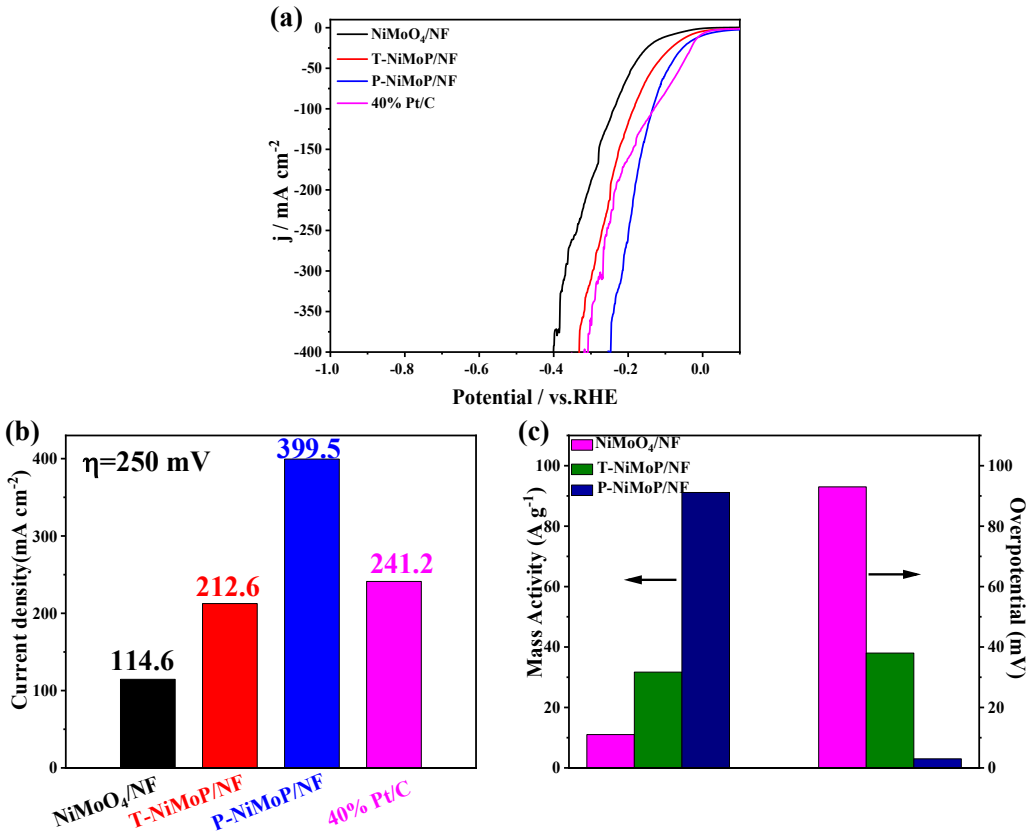

Fig. S6 (a) Polarization curves at high current density. (b) Current density at the overpotential of 250 mV, (c) Comparison of mass activity at 100 mV and overpotential at 10 mA cm^{-2} for $NiMoO_4$/NF, T-NiMoP/NF and P-NiMoP/NF.

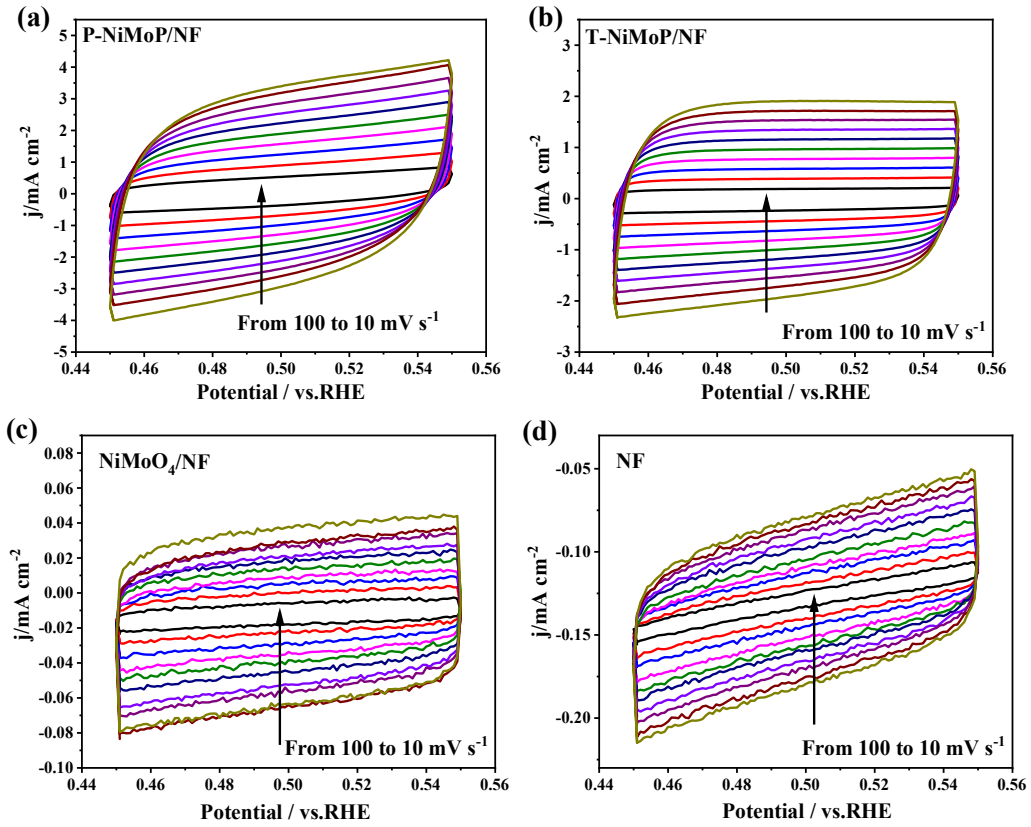

Fig. S7 CVs of (a) P-NiMoP/NF, (b) T-NiMoP/NF, (c) $NiMoO_4$/NF, and (d) NF electrodes at the potential regions of 0.45 and 0.55 V (vs. RHE) with scan rates of 10-100 mV s^{-1} in 1.0 M KOH solution.

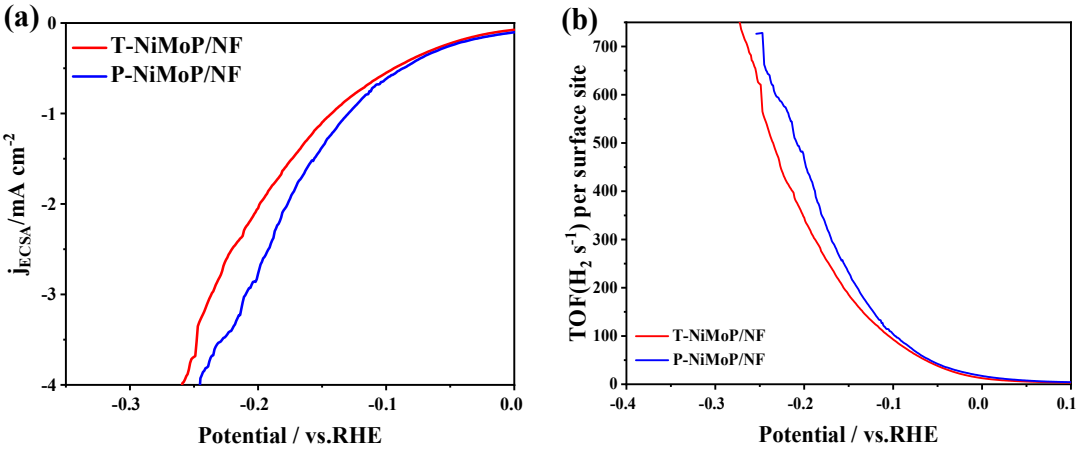

Fig. S8 (a) ECSA normalized polarization curves. (b) Overpotential dependent TOFs.

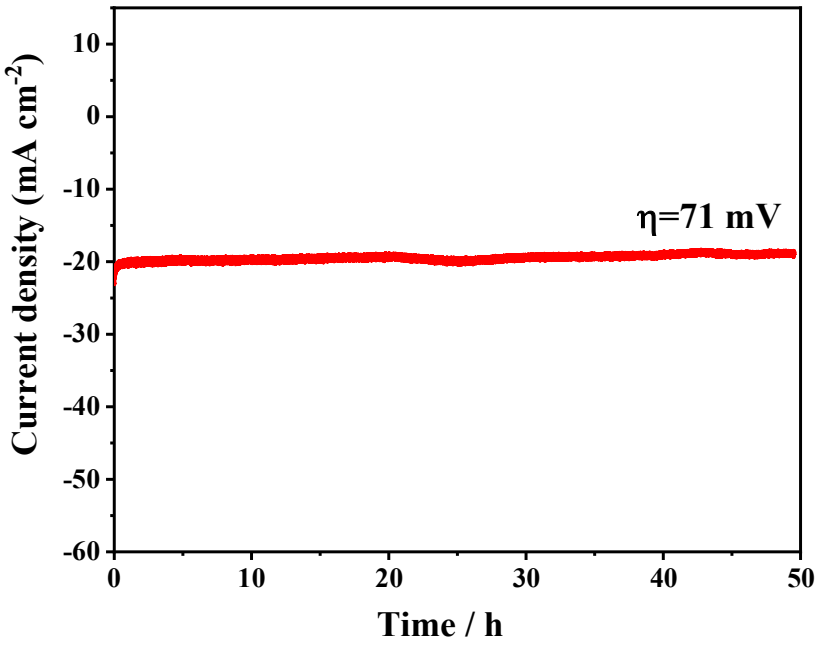

Fig. S9 Current density during electrolysis for P-NiMoP/NF in 1.0 M KOH at η=71 mV.

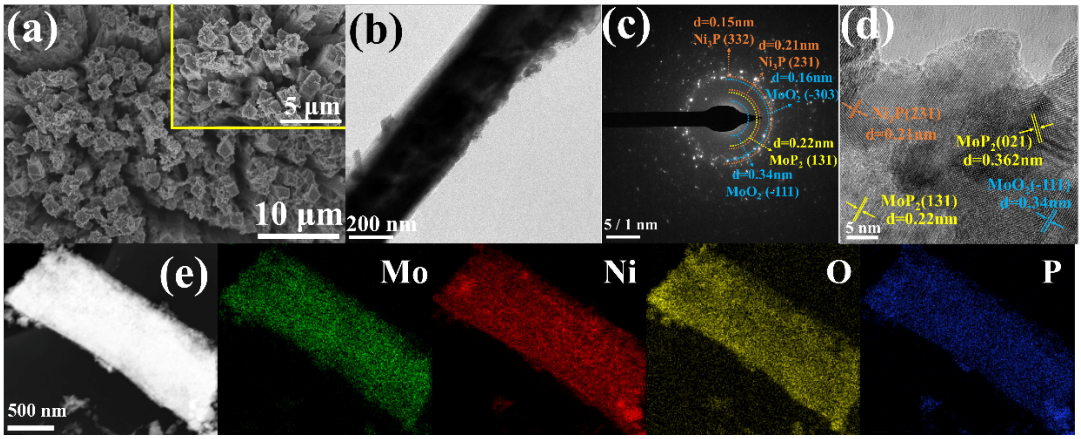

Fig. S10 (a) SEM images, (b) TEM image, (c) SAED pattern, (d) HRTEM image and (e) EDX elemental mapping images of P-NiMoP after HER stability testing.

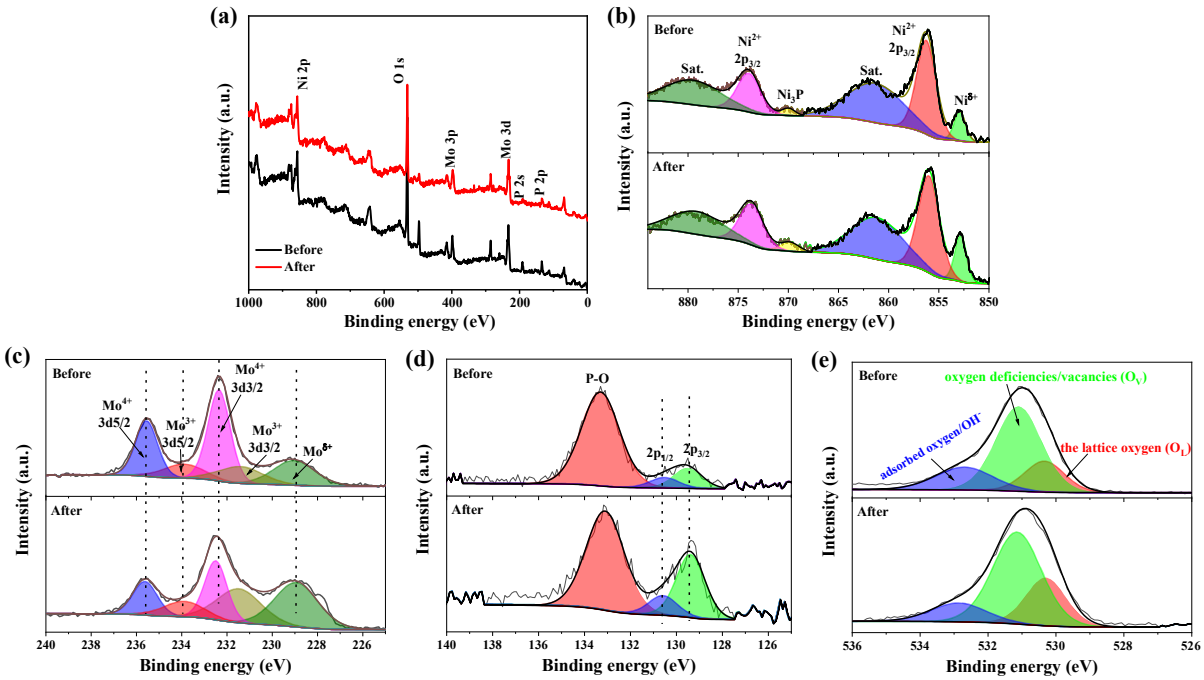

Fig. S11 (a) XPS survey of P-NiMoP. High-resolution XPS spectra of (b) Mo 3d, (c) Ni 2p, (d) P 2p, (e) O 1s of P-NiMoP before and after stability testing.

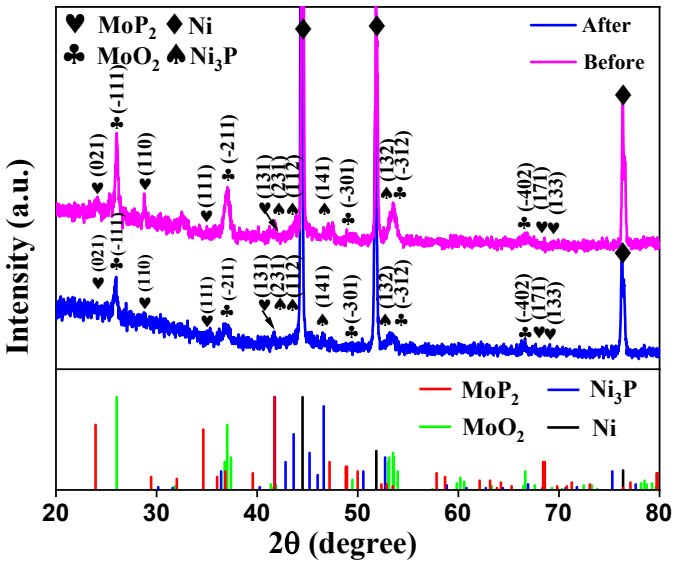

Fig. S12 XRD patterns of P-NiMoP/NF before and after the stability test for 50 h at the overpotential of 71 mV *vs*. RHE.

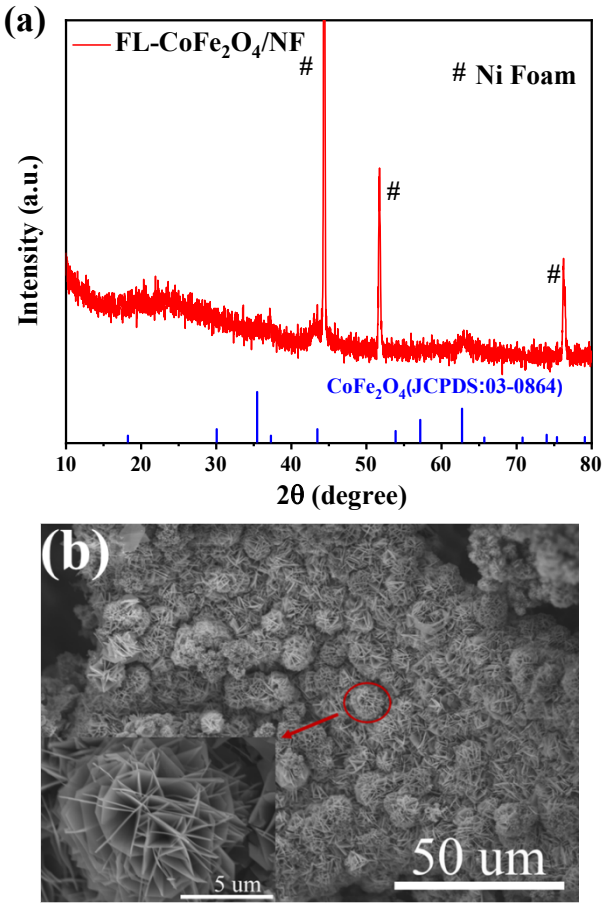

Fig. S13 (a) XRD pattern and (b) SEM images of FL-$CoFe_2O_4$/NF.

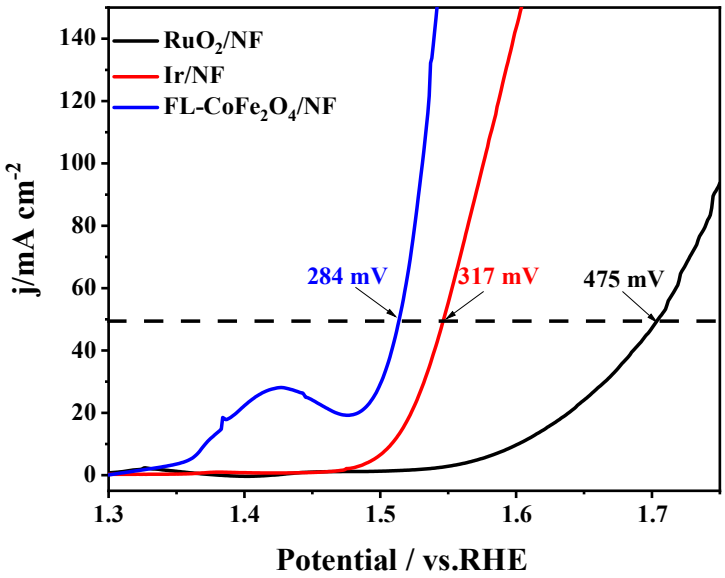

Fig. S14 LSV OER polarization curves of RuO_2/NF, Ir/NF, and FL-$CoFe_2O_4$/NF in 1 M KOH.

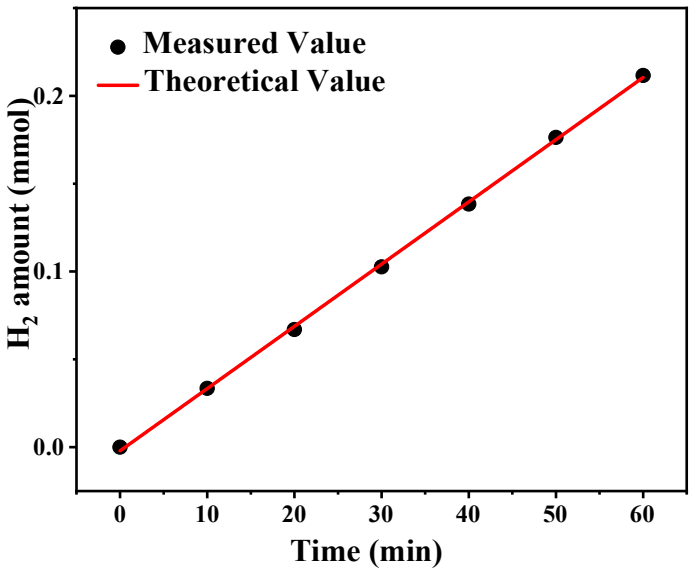

Fig. S15 Amounts of H_2 generated (the black dots) by FL-$CoFe_2O_4$/NF(+)||P-NiMoP/NF(-) under the current density of 10 mA cm^{-2} in 1.0 M KOH. The straight line represents of the theoretical amount of H_2 that can be generated with a Faradiac efficiency of 100%.

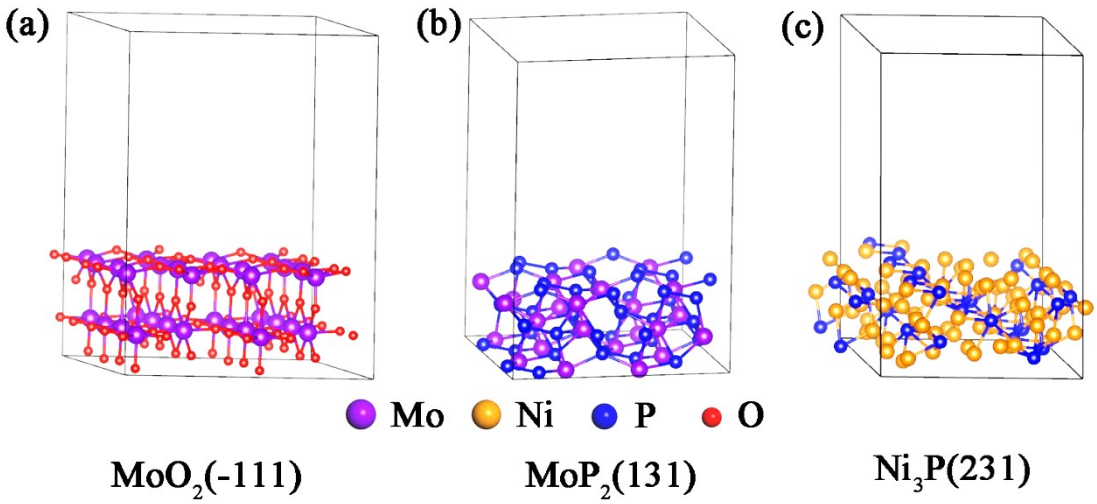

Fig. S16 Structures of MoO_2 (-111), MoP_2(131), and Ni_3P(231) used for the DFT calculations.

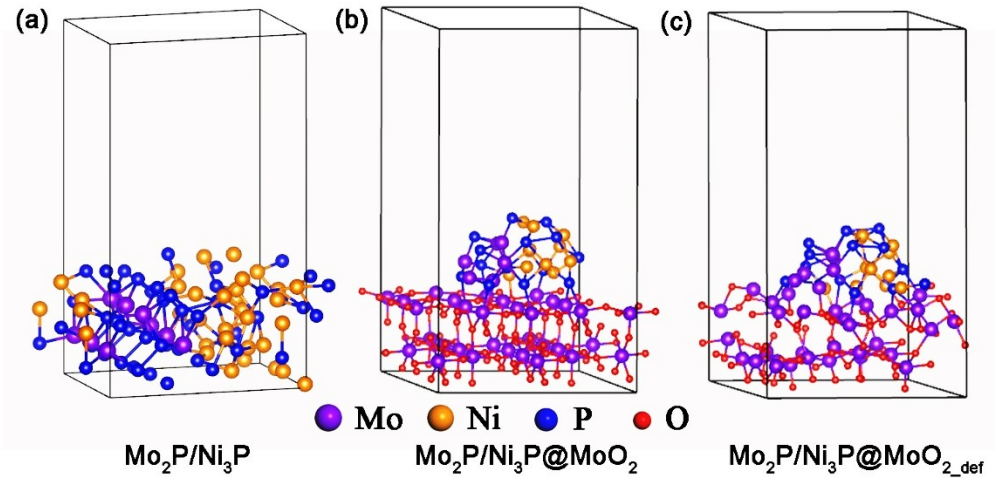

Fig. S17 Heterostructures of MoP_2/Ni_3P, $MoP_2/Ni_3P@MoO_2$ and $MoP_2/Ni_3P@MoO_{2\_def}$ used for the DFT calculations.

Table S1. Comparison of electrocatalytic HER activity of various nonprecious catalysts in different electrolyte.

Catalysts	Electrolytes	η(mV)@ J(mA cm^{-2})	Tafel slope (mV dec^{-1})	j_0/μA cm^{-2}	TOF(η_{100})(s^{-1})	Stability(h) @η(mV)	Stability(h) @j(mA cm^{-2})	Ref.
P-NiMoP/NF	1.0M KOH	3@10 131@100 162@150	65.7	8560	104.0	50@71	12@10 12@100	This Work
P-CoMoO$_4$/NF	1.0M KOH	94@10 197@100	94	NA	NA	48@150	NA	[1]
P-doped βCoMoO$_4$	1.0M KOH	138@10	68.8	NA	NA	20@138	NA	[2]
Co$_4$NiP	1.0M KOH	129@10	52	NA	NA	20@188 20@188	NA	[3]
Co$_{0.93}$Ni$_{0.07}$P$_3$ /CC	1.0M KOH	87@10	60.7	NA	NA	NA	10@20	[4]
Ni$_{2(1-x)}$Mo$_{2x}$P	1.0M KOH	72@10 162@100	46.4	537	0.038	100@110	NA	[5]
P-Mo-Ni(OH)$_2$	1.0M KOH	22@10 98@100	80	NA	NA	100@100	NA	[6]
N-NiCoP/NCF	1.0M KOH	78@10	83.2	NA	9.786×10^{-3}	NA	100@10	[7]
NiFe LDH@NiCoP/NF	1.0M KOH	120@10	88.2	NA	NA	NA	100@10	[8]
Ni$_{2-x}$Cu$_x$P/NF	1.0M KOH	78@10 245@100	70	NA	NA	NA	30@10	[9]
N-NiVFeP/NFF	1.0M KOH	79@10	78.6	NA	NA	NA	100@10 100@100	[10]
NiMoN/CC	1.0M KOH	109@10	95	920	NA	NA	12@10 12@30 12@50	[11]
C-NiMoO$_4$/CC	1.0M KOH	76@10	78	NA	NA	NA	12@10 12@30 12@50	[12]
Fe-CoP/Ti	1.0M KOH	78@10	75	NA	NA	20@10	NA	[13]
NiCoP/CC	1.0M KOH	62@10	67	NA	NA	15@20	NA	[14]
Cu@NiFe LDH	1.0M KOH	116@10 192@100	58.9	NA	NA	48@162	48@10 24@100	[15]
MoP/SN	1.0M KOH	94@10 132@20	59.7	480	NA	NA	20@10	[16]
CoP/C	1.0M KOH	163@10	101	NA	NA	10@163	NA	[17]

NA: Not available

Table S2. Catalytic performance comparison of the catalysts.

Catalysts	HER				EASA / cm^{-2}	Charge transfer resistance (R_{ct}) (Ω)
	η_{10} / mV	Tafel slope / mV dec^{-1}	j_0 / μA cm^{-2}	C_{dl} / mF cm^{-2}		
$NiMoO_4$/NF	93	148.2	2340	1.49	2.29	19.06
T-NiMoP/NF	38	139.1	6120	37.45	57.62	10.21
NF	115	173	NA	0.65	1	NA
P-NiMoP/NF	3	65.7	8560	60.21	92.63	4.17
Pt/C	9	57.7	7190	NA	NA	NA

Table S3. The turnover frequency (TOF) of the T-NiMoP and P-NiMoP.

	η=100 mV	η=150 mV	η=200 mV
T-NiMoP	92.8 s^{-1}	185.4 s^{-1}	345.4 s^{-1}
P-NiMoP	104.0 s^{-1}	231.4 s^{-1}	467.2 s^{-1}

Table S4. Comparison of the overall water splitting activity of the combination of P-NiMoP and FL-$CoFe_2O_4$/NF with other efficient hetero and bifunctional catalysts in 1 M alkaline electrolytes.

Catalysts	Electrolytes	Voltage (V) at the corresponding j (mA cm^{-2})	References
P-NiMoP/NF	1.0 M KOH	1.41@10 1.58@50 1.63@100	This Work
P-Mo-Ni(OH)$_2$	1.0 M KOH	1.51@10 1.78@100	6
N-NiCoP/NCF	1.0 M KOH	1.56@10	7
N-NiVFeP/NFF	1.0 M KOH	1.52@10	10
Cu@NiFe LDH	1.0 M KOH	1.54@10 1.69@100	15
$F_{0.25}C_1$CH/NF	1.0 M KOH	1.45@10 1.49@100	18
Cu@CoS_x/CF	1.0 M KOH	1.50@10 1.80@100	19
$NiMoP_2$	1.0 M KOH	1.60@10 1.94@50	20
NiSe/NF	1.0 M KOH	1.63@10 1.74@20	21
FeCoNi-HNTAs	1.0 M KOH	1.429@10 1.61@50 1.73@100	22

References

1. S. Zhao, J. Berry-Gair, W. Li, G. Guan, M. Yang, J. Li, F. Lai, F. Corà, K. Holt, D. J. L. Brett, G. He and I. P. Parkin, *Adv. Sci.*, 2020, **7**, 1903674.
2. S. Li, N. Yang, L. Liao, Y. Luo, S. Wang, F. Cao, W. Zhou, D. Huang and H. Chen, *ACS Appl. Mater. Interfaces*, 2018, **10**, 37038-37045.
3. L. Yan, L. Cao, P. Dai, X. Gu, D. Liu, L. Li, Y. Wang and X. Zhao, *Adv. Funct. Mater.*, 2017, **27**, 1703455.
4. Q. Fu, T. Wu, G. Fu, T. Gao, J. Han, T. Yao, Y. Zhang, W. Zhong, X. Wang and B. Song, *ACS Energy Lett.*, 2018, **3**, 1744-1752.
5. L. Yu, I. K. Mishra, Y. Xie, H. Zhou, J. Sun, J. Zhou, Y. Ni, D. Luo, F. Yu, Y. Yu, S. Chen and Z. Ren, *Nano Energy*, 2018, **53**, 492-500.
6. W. Zhang, Y. Tang, L. Yu and X.-Y. Yu, *Appl. Catal. B-Environ.*, 2020, **260**, 118154.
7. R. Zhang, J. Huang, G. Chen, W. Chen, C. Song, C. Li and K. Ostrikov, *Appl. Catal. B-Environ.*, 2019, **254**, 414-423.
8. H. Zhang, X. Li, A. Hähnel, V. Naumann, C. Lin, S. Azimi, S. L. Schweizer, A. W. Maijenburg and R. B. Wehrspohn, *Adv. Funct. Mater.*, 2018, **28**, 1706847.
9. S. Chu, W. Chen, G. Chen, J. Huang, R. Zhang, C. Song, X. Wang, C. Li and K. Ostrikov, *Appl. Catal. B-Environ.*, 2019, **243**, 537-545.
10. H. Fan, W. Chen, G. Chen, J. Huang, C. Song, Y. Du, C. Li and K. Ostrikov, *Appl. Catal. B-Environ.*, 2020, **268**, 118440.
11. Y. Zhang, B. Ouyang, J. Xu, S. Chen, R. S. Rawat and H. J. Fan, *Adv. Energy Mater.*, 2016, **6**, 1600221.
12. Y. Zhang, B. Ouyang, K. Xu, X. Xia, Z. Zhang, R. S. Rawat and H. J. Fan, *Small*, 2018, **14**, 1800340.
13. C. Tang, R. Zhang, W. Lu, L. He, X. Jiang, A. M. Asiri and X. Sun, *Adv. Mater.*, 2017, **29**, 1602441.
14. C. Du, L. Yang, F. Yang, G. Cheng and W. Luo, *ACS Catal.*, 2017, **7**, 4131-4137.
15. L. Yu, H. Zhou, J. Sun, F. Qin, F. Yu, J. Bao, Y. Yu, S. Chen and Z. Ren, *Energy Environ. Sci.*, 2017, **10**, 1820-1827.
16. M. A. R. Anjum and J. S. Lee, *ACS Catal.*, 2017, **7**, 3030-3038.
17. B. Luo, T. Huang, Y. Zhu and D. Wang, *J. Energy Chem.*, 2017, **26**, 1147-1152.
18. L. Hui, Y. Xue, D. Jia, H. Yu, C. Zhang and Y. Li, *Adv. Energy Mater.*, 2018, **8**, 1800175.
19. Y. Liu, Q. Li, R. Si, G.-D. Li, W. Li, D.-P. Liu, D. Wang, L. Sun, Y. Zhang and X. Zou,

Adv. Mater., 2017, **29**, 1606200.

20. X.-D. Wang, H.-Y. Chen, Y.-F. Xu, J.-F. Liao, B.-X. Chen, H.-S. Rao, D.-B. Kuang and C.-Y. Su, *J. Mater. Chem. A*, 2017, **5**, 7191-7199.
21. C. Tang, N. Cheng, Z. Pu, W. Xing and X. Sun, *Angew. Chem. Int. Ed.*, 2015, **54**, 9351-9355.
22. H. Li, S. Chen, Y. Zhang, Q. Zhang, X. Jia, Q. Zhang, L. Gu, X. Sun, L. Song and X. Wang, *Nat. Commun.*, 2018, **9**, 2452.